Local amplification of deep mining induced vibrations part.2: Simulation of ground motion in a coal basin

Jean-François Semblat, Nabila Lokmane, Lynda Driad-Lebeau, Guy Bonnet

Local amplification of deep mining induced vibrations part.2: Simulation of ground motion in a coal basin

J.F. Semblat [a,*], N. Lokmane [a,c], L. Driad-Lebeau [b], G. Bonnet [c]

[a] Université Paris-Est, LCPC, Department of Soil and Rock Mechanics, Engineering Geology, 58 bd Lefebvre, 75015 Paris, France
[b] Institut National de l'Environnement Industriel et des Risques (INERIS), Ecole des Mines, Parc Saurupt 54042 Nancy, France
[c] Université Paris-Est, Laboratoire de Modélisation et Simulation Multi-Echelle LMSME (CNRS UMR 8208), France

A B S T R A C T

This work investigates the impact of deep coal mining induced vibrations on surface constructions using numerical tools. An experimental study of the geological site amplification and of its influence on mining induced vibrations has already been published in the previous paper (Part 1: Experimental evidence for site effects in a coal basin). Measurements have shown the existence of an amplification area in the southern part of the basin where drilling data have shown the presence of particularly fractured and soft stratigraphic units. The present study, using the boundary element method (BEM) in the frequency domain, first investigates canonical geological structures in order to get general results for various sites. The amplification level at the surface is given as a function of the shape of the basin and of the velocity contrast with the bedrock. Next, the particular coal basin previously studied experimentally (Driad-Lebeau et al. [1]) is modeled numerically by BEM. The amplification phenomena characterized numerically for the induced vibrations are found to be compatible with the experimental findings such as: amplification level, frequency range and location. Finally, the whole work was necessary to fully assess the propagation and amplification of mine induced vibrations. The numerical results quantifying amplification can also be used to study other coal basins or various types of alluvial sites.

Keywords:
Site effects
Vibration
Coal mine
Seismic wave
Induced vibrations
Amplification
Boundary element method

1. Mine induced vibrations

As shown in Driad-Lebeau et al. [1], mining operations may induce a redistribution of the stress field based on the mechanical behavior of the rockmass. This can lead to a substantial microseismic activity [2–7]. The rupture process generates elastic waves, which are propagated through the geological structure up to the free surface. Seismic monitoring was thus performed in numerous mines [1]. In recent years, the impact of mine induced vibrations on surface constructions (i.e. houses or buildings located close to a mine) has been studied. This type of dynamic loading is different from seismic excitations coming from natural earthquakes (return period, amplitude, frequency range, etc.).

Detailed studies were carried out for a coal basin in the framework of a French research program called "SisMine" initiated by INERIS and sponsored by the French collieries [1]. LCPC and University Paris-Est-Marne la Vallée were associated with this research program in order to develop a numerical methodology aimed at simulating the impact on surface constructions of weak amplitude vibrations. The SisMine research program is subdivided into three parts, each one devoted to specific goal as following: Part 1: experimental estimation of site effects in the coal basin [1]; Part 2: numerical estimation of site effects in the coal basin and comparison with experimental results (present paper) and Part 3: impact of deep mining vibration on surface constructions—numerical approach.

This paper numerically investigates the propagation and amplification of mine induced vibrations in coal basins. It consists in a general study of various basin geometries (canonical basins) and detailed analyses of the Gardanne coal basin (Provence, France). Comparisons with experimental results from the field are also proposed.

2. Experimental analysis in the field

2.1. Site description

The Gardanne basin is located between Aix-en-Provence and Marseille (South of France) several kilometers westward from the city of Gardanne (latitude: 43° 27′ 16″ North and longitude: 5° 28′ 34″ East). It overlays a coalfield which forms the eastern part of the arc basin and constitutes an E–W oriented geological unit (Gaviglio et al., 1996) [37]. The general tectonic features and

* Corresponding author.
E-mail addresses: semblat@lcpc.fr (J.F. Semblat), Lynda.Driad-Lebeau@ineris.fr (L. Driad-Lebeau), guy.bonnet@univ-paris-est.fr (G. Bonnet).

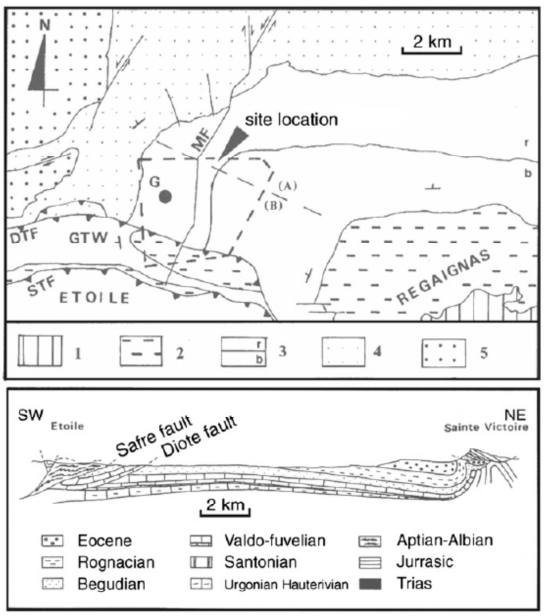

Fig. 1. *Top*: geological setting and location of Gardanne colliery (1: Upper Jurassic; 2: Campanian; 3: Begudian and Rognacian (3b,3r); 4: Eocene; 5: Oligocene). The coalfield is located in the Campagnian limestones. *Bottom*: geological cross-section of the Gardanne basin *[after Driad-Lebeau et al., 2009]*.

geological setting of the basin are quite simple (Fig. 1). The Gardanne basin is composed of a fluvio-lacustrine of the upper Cretaceous and the Eocene overlaying a substratum of the Jurassic (or lower cretaceous). The stratigraphy sequence consists mainly in marls, limestones and sandstones of the Valdonnian together with limestones of the Fuvelian (hard and brittle) with intermediate lignites (Fig. 1). The shallower sequences are represented by clay–sandy limestones of the Rognacian and Begudian. The presence on the surface of marine abrasion and molasses deposits has marked the influence of a sedimentary episode of the Miocene.

Among the 8 coal levels having been exploited since the Middle Ages, the last seam mined until the closing of the mine (2003) was the so-called "Grande Mine". That is the most significant layer (2.5 m thick) located at depths ranging from 1000 to 1400 m. The coal layers were worked with a long wall caving method that uses two roadways and extracts coal along a straight front having a large longitudinal extension. The stoping area close to the face is kept open to provide a security zone for the staff and the mining equipment.

2.2. Experimental results on induced vibrations

The seismic events induced by mining exploitation were recorded by using the mobile network described in [1]. These data have been processed in the frequency domain and all events of magnitude greater than 2.5 have been considered (mine depth is approximately 1 km). Such events constitute the vibrations of interest in terms of impact on surface constructions. In Fig. 2, *H/V* spectral ratios from mine induced vibrations recordings were computed for 10-instrumented sites (8 residences and 2 free-surface sites). They are plotted as average *H/V* spectral ratios plus/minus one standard deviation.

As shown in Fig. 2, the *H/V* spectral ratios highlight significant variations in resonances and amplitude peaks (evidencing amplification) at the investigated sites. Spectral ratios above 8 are found in the frequency band 3–8 Hz at sites FOU, LER, LAG and MON and NAY (see [1] for these various locations). The sites HEN and NAY, where outcrops are mainly marl-limestone, present a weak resonance (amplitude of nearly 3–4) at 3–6 Hz. This observation is coherent with the geological setting where the limestone dominates. In this particular case, the amplification effect is not very significant. It is interesting to note the response of the site MON, which presents a broad resonance at 4.5 Hz with an amplitude of 7. Indeed, according to the geology (limestone-marls), the *H/V* ratio would be expected close to that of the site HEN. It suggests that the observed amplitude could be related to a topographic effect. Indeed, the corresponding house is located on the slope of a hill, which culminates at 210 m.

3. Modeling wave propagation in soils

3.1. Numerical methods for wave propagation

To analyze wave propagation (seismic waves, vibrations, etc.) in 2D or 3D geological structures, various numerical methods are available:

- the finite difference method is accurate in elastodynamics but free surface or interface conditions has to be carefully considered [8,9],
- the finite element method is efficient to deal with complex geometries and numerous heterogeneities (even for inelastic constitutive models [10]) but has several drawbacks such as numerical dispersion (error in terms of phase velocity) and numerical damping [11–14]) and (consequently) numerical cost in 3D elastodynamics,
- the spectral element method has been increasingly considered to analyze 2D/3D wave propagation in linear media with a good accuracy due to its spectral convergence properties [15–17],
- the boundary element method allows a very good description of the radiation conditions but is preferably dedicated to weak heterogeneities and linear constitutive models [18–21]. Recent developments have been proposed to reduce the computational cost of the method especially in the high frequency range [22–24],
- the Aki-Larner method which takes advantage of the frequency–wavenumber decomposition [25,26],
- the scaled boundary finite element method which is a kind of solution-less boundary element method [27],
- other methods for simple geometries such as series expansions of wave functions [28].

Furthermore, when dealing with wave propagation in unbounded domains, many of these numerical methods require absorbing boundary conditions to avoid spurious reflections [14,15]. For instance, it is possible to couple FEM and BEM [19,29] allowing an accurate description of the near field (FEM model including complex geometries, numerous heterogeneities and nonlinear constitutive laws) and a reliable estimation of the far-field (BEM involving accurate radiation conditions).

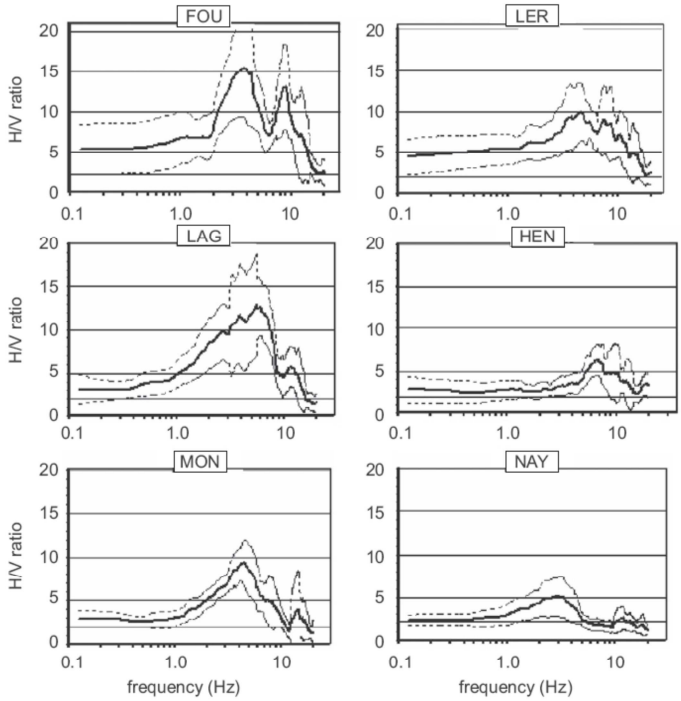

Fig. 2. *H/V* spectral ratios from mining induced seismic data. Thick line: average *H/V* ratios for each recording location, dotted line: plus/minus one standard deviation.

3.2. The boundary element method

The main advantage of the boundary element method is to avoid artificial truncation of the domain in the case of an infinite medium. For dynamic problems, this truncation leads to artificial wave reflections giving a numerical error in the solution. The boundary element method can be divided into two main stages [19]:

- solution of the boundary integral equation giving displacements and stresses along the boundary of the domain,
- a posteriori computation for all points inside the domain using an integral representation formula.

The boundary element method arises from the application of the Maxwell–Betti reciprocity theorem leading to the expression of the displacement field inside the domain Ω from the displacements and stresses along the boundary $\partial\Omega$ of the domain [19].

3.3. Elastodynamics

We consider an elastic, homogeneous and isotropic solid of volume Ω and external surface $\partial\Omega$. Within this medium, the equation of motion can be written under the following form:

$$(\lambda+2\mu)\mathit{grad}(\mathit{div}\boldsymbol{u})-\mu\mathit{rot}(\mathit{rot}\boldsymbol{u})+\rho f=\rho\ddot{u} \tag{1}$$

where λ and μ are the Lamé coefficients, $\mathbf{u}$ the displacement field, ρ the mass density and $\boldsymbol{f}$ a force density.

By using the Fourier transform, the problem can be studied in the frequency domain, for each circular frequency ω. The equation of motion for a steady state $(\mathbf{u}(x), \boldsymbol{\sigma}(x))$ can then be written as follows:

$$(\lambda+2\mu)\mathit{grad}(\mathit{div}\boldsymbol{u}(x))-\mu\mathit{rot}(\mathit{rot}\boldsymbol{u}(x))+\rho f(x)+\rho\omega^2 u(x)=0 \tag{2}$$

This equation is written in the framework of linear elasticity but, since the analysis is performed in the frequency domain, damped mechanical properties may be considered through the complex modulus of the medium [14].

3.4. Integral representation

For steady solutions of harmonic problems, the reciprocity theorem between two elastodynamic states comprising displacement fields and stress fields $(\mathbf{u}(x), \boldsymbol{\sigma}(x))$ in equilibrium with body forces $\mathbf{f}(x)$ and $(\mathbf{u}'(x), \boldsymbol{\sigma}'(x))$ in equilibrium with body forces $\mathbf{f}'(x)$ takes the following form:

$$\int_{\partial\Omega}\boldsymbol{t}^{(n)}(x)\boldsymbol{u}'(x)\,ds(x)+\int_{\Omega}\rho\boldsymbol{f}(x)\boldsymbol{u}'(x)\,dv(x) = \int_{\partial\Omega}\boldsymbol{t}'^{(n)}(x)\boldsymbol{u}(x)\,ds(x)+\int_{\Omega}\rho\boldsymbol{f}'(x)\boldsymbol{u}(x)\,dv(x) \tag{3}$$

The integral formulation is obtained through the application of the reciprocity theorem between the elastodynamic state $(\boldsymbol{u}(x), \boldsymbol{\sigma}(x))$ and the fundamental solutions of a reference problem called Green kernels. The reference problem generally corresponds to the infinite full space case in which a volumic concentrated force at point y acts in the direction $\mathbf{e}$. In the harmonic case, the Green kernel of the infinite medium corresponds to a volumic force field such as

$$\rho\boldsymbol{f}'(x)=\delta(x-y)\boldsymbol{e} \tag{4}$$

In this article, the model involves the Green functions of an infinite medium ([19]) or semi-infinite medium (in the case of SH-waves). The Green kernel is denoted $U_{ij}^{\omega}(x,y)$ and characterizes the complex displacement in the direction j at point x due to a unit (time harmonic) force concentrated at point y along the direction i. The corresponding traction on a surface of normal vector $n(x)$ is denoted by $T_{ij}^{(n)\omega}(x,y)$. The application of the reciprocity theorem between the elastodynamic state ($\mathbf{u}(x)$, $\boldsymbol{\sigma}(x)$) and that defined by the Green kernel $U_{ij}^{\omega}(x,y)$ gives the following integral representation:

$$I_{\Omega}(y)u_i(y) = \int_{\partial\Omega} (U_{ij}^{\omega}(x,y)t_j^{(n)}(x) - T_{ij}^{(n)\omega}(x,y)u_j(x))\,ds(x) + \int_{\Omega} \rho U_{ij}^{\omega}(x,y)f_j(x)\,dv(x) \quad (5)$$

where $I_{\Omega}(y)$ is 1 when y is inside Ω and 0 when it is outside Ω.

Numerical solution of Eq. (5) can be performed by a collocation method or by an integral variational approach [19].

3.5. Regularization and discretization of the problem

The integral representation defined by Eq. (5) is generally not valid for $x \in \partial\Omega$. The formulation of the boundary integral equation along $\partial\Omega$ is then not very easy to obtain as the Green kernels have singular values when $x \in \partial\Omega$. It is then necessary to regularize expression Eq. (5) to write the boundary integral equation [18–20].

The problems presented in this article are analyzed in two dimensions (plane or anti-plane strains). Two-noded boundary elements are chosen and the element size corresponds to one-tenth of the minimum wavelength. Two dimensional Green kernels of the infinite space are written using Hankel's functions [19]. The regularized solution of Eq. (5) is estimated by classical boundary finite elements discretization and then by collocation method, that is application of the integral equation at each node of the mesh.

4. Wave amplification in simple alluvial structures

Many different authors have studied the propagation and amplification of seismic waves in alluvial structures [21,30,31,32,40,41]. In such geological structures, the seismic motion may be amplified due to the velocity contrast between the various layers and to the limited geometrical extent of the basin (trapped surface waves). For mine induced vibrations, this phenomenon may also occur and significantly modify the ground motion at the free surface. We will thus analyze ground motion amplification, in a first step for simplified geological structures and next for the actual profile of the Gardanne coal basin.

4.1. Preliminary analysis for various geological deposits

Few geotechnical data are available for the Gardanne coal basin and we thus performed a parametric study making our results useful for other sites. Various geometries have been chosen for the deposit with variable mechanical properties. The incident wavefield is a plane vertical SH wave. The numerical simulations involve the boundary element method (FEM–BEM code CESAR–LCPC [33]).

The amplification of seismic waves in alluvial deposits is strongly influenced by the mechanical properties of the latter. Indeed the velocity contrast between soil layers governs the ground motion at the free surface. The geometry of the deposit is also an important factor. It may be characterized by its mean depth or in a more detailed way for alluvial basins. Due to the lateral heterogeneities, the seismic waves are trapped in the basin, leading to a large motion amplification. In the one-dimensional case (horizontal layers), a close-form solution can be obtained for the amplification factor of the ground motion [14]. Conversely, when the lateral heterogeneities are strong, 2D or 3D wave propagation must be considered.

4.2. Horizontal layering

We first consider the case of a simplified deposit involving a single horizontal layer. The layer depth is estimated from the Simiane 2 (SI 2) borehole giving an approximate depth but no detailed information about the layer geometry [1]. The fundamental solution for the half space is considered and a vertically incident plane wave is propagated in the bedrock. The simplified geometry is defined as follows:

- Layer depth $H=15$ m and width $L=3000$ m;
- Layer and bedrock properties (subscript L and b, respectively):
  - Case 1: bedrock/layer velocity contrast $V_{Sb}/V_{SL}=12$;
  - Case 2: bedrock/layer velocity contrast $V_{Sb}/V_{SL}=4$.

As displayed in Fig. 3, the maximum amplification factor is 16.75 in Case 1 (reached at $f=1.8$ Hz) and 5.0 in Case 2 (at $f=4.4$ Hz). As shown by these results (also see closed-form solutions in [14]), the ground motion amplification is strongly influenced by the velocity contrast between the soil layer and the bedrock.

When comparing these results to the 1D closed-form solutions, the former are approximately 40% larger than the latter. The geometrical extent of the deposit also has a strong influence on the ground motion amplification. In the following, we will thus analyze the influence of the basin geometry on the motion amplification.

4.3. Influence of the basin geometry

4.3.1. Variable shape ratio

The influence of the basin geometry is assessed by considering elliptical basins with different geometrical extents (i.e. shape ratios). As shown in Fig. 4, the basins are characterized by their half-width L, their depth H and their shear wave velocity V_{S1} ($V_{S2} > V_{S1}$ being the shear velocity in the bedrock). Various geometries are considered: narrow basins ($L < H$) as well as large ones ($L > H$).

In order to use these results for various alluvial sites, the parametric study is performed considering such dimensionless parameters as: the amplification factor A, the horizontal shape ratio $\kappa_h = L/H$ ($\kappa_h=1$ for the circular geometry), the velocity ratio $\chi = V_{S2}/V_{S1}$ and the dimensionless frequency $\eta_v = H/\lambda$ (ratio between basin depth and wavelength).

4.3.2. Comparison between the 1D case and the circular basin

Considering an alluvial deposit of constant thickness overlying an elastic bedrock, the transfer function of the ground motion across the soil layer may be derived as a closed-form solution [14]. For a plane SH wave, the modulus of the transfer function is:

$$|T_{1,2}^{*}(\omega)| = [\cos^2 k_{z1}H + \overline{\chi}^2 \sin^2 k_{z1}H]^{-1/2} \quad (6)$$

where $k_{z1} = \omega \cos\alpha_1 / V_{S1}$ is the horizontal wavenumber and $\overline{\chi} = \sqrt{(\rho_1\mu_1/\rho_2\mu_2)}(\cos\alpha_1/\cos\alpha_2)$ with ω the frequency, α_1 and α_2 the angles between the direction of propagation of the wave and the vertical axis in the layer and in the bedrock, respectively (α_1 is estimated from α_2 [14]). H is the layer depth, μ_1, μ_2 are the

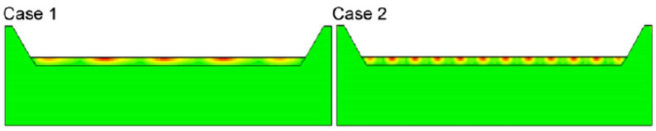

Fig. 3. Ground motion amplification in the alluvial deposit. Maximum amplification is obtained in the surficial layer. Case 1 (left): maximum amplification 16.75 at $f=1.8$ Hz; Case 2 (right): maximum amplification 5.0 at $f=4.4$ Hz.

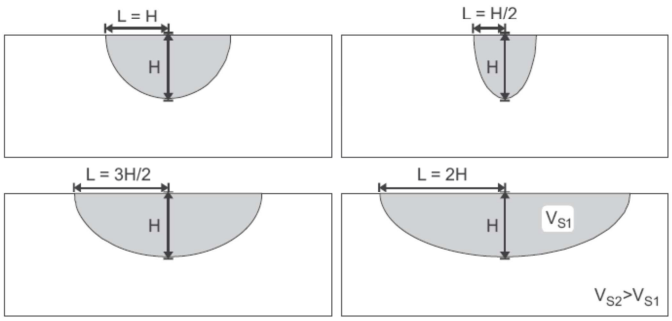

Fig. 4. Elliptical basins of variable shape ratio $\kappa_h=L/H$.

shear moduli and ρ_1, ρ_2 are the mass densities (indices 1 and 2 for the layer and bedrock, respectively.).

Eq. (6) corresponds to the amplification factor of the ground motion: the amplitude at the top of the layer is divided by the so-called outcrop motion (amplitude at the surface of the bedrock without the alluvial deposit).

From Eq. (6), the dimensionless frequency giving the maximum amplification is found to be $\eta_v=0.25$ (i.e., quarter-wavelength resonance) whereas, for the circular basin, the maximum amplification is reached at $\eta_v=0.35$ [14]. The different is due to the 2D basin effects (lateral heterogeneities). We will now investigate the influence of the basin shape on the amplification level.

5. Variable basin shape: parametric study

For a plane SH-wave, various elliptical basins are considered (Fig. 4). Their horizontal shape ratios, $\kappa_h=L/H$, are chosen as κ_h=0.5; 1; 2; 3; 4; 5 and 6 (the basin depth being constant: H=25m). Different velocity ratios were also chosen: χ=2–8. From all these models, the maximum motion amplification and the related frequency were computed. The results are plotted in Fig. 5 as an abacus: solid lines correspond to fixed shape ratios κ_h and dotted lines to constant velocity ratios χ. The main conclusions are the following:

- For a constant velocity ratio and shape ratios larger than 1, the maximum amplification and the related frequency decrease when increasing shape ratio and the results are becoming closer to the 1D case.
- For narrow basins (small shape ratios), the 2D results are far from the 1D analysis (strong 2D effects).
- For a constant shape ratio, when the velocity ratio increases, the maximum amplification increases and the related frequency decreases.

From Fig. 5, it is thus possible to estimate the maximum ground motion amplification and the related frequency for various types of alluvial basins. For instance, if we consider

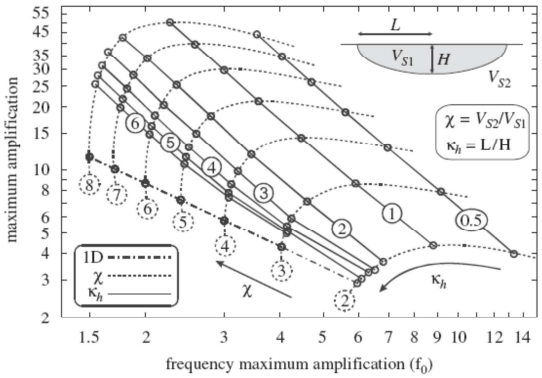

Fig. 5. Maximum amplification and related frequencies (in Hz) for variable shape ratios $\kappa_h=L/H$ and velocity ratios $\chi=V_{S2}/V_{S1}$.

κ_h=1.5 and χ=3.5, the maximum amplification is above 10 and the related frequency is around 4.5.

Our numerical results for an elliptical basin were compared to Bard and Bouchon's results (1985) for sinusoidal basins in terms of fundamental frequencies. Bard and Bouchon [34] proposed the following empirical law:

$$f_{2D}=\left(\frac{V_{S1}}{4H}\right)\sqrt{1+\kappa_v^2} \tag{7}$$

where $\kappa_v=1/\kappa_h=H/L$ is the vertical shape ratio defined by Bard and Bouchon, L is the basin half width, H is the basin depth and V_{S1} is the velocity in the basin.

When compared to Bard and Bouchon's results, our frequencies of maximum amplification have similar variations with respect to the shape ratio. 2D effects are found to be strong for narrow basins whereas large basins lead to amplification levels close to the 1D case.

The ground motion amplifications are computed in the frequency domain (time harmonic signal). Time domain computations will be proposed in the following.

6. Numerical analysis for the Gardanne coal basin

6.1. Coal basin profile

For the Gardanne coal basin (Fig. 1), a North–South profile has been defined (Fig. 6) along which four drillings have been performed (F_1, F_2, F_3 and F_4). A boundary element model (FEM–BEM code CESAR–LCPC) has been prepared from this profile (Fig. 6, bottom). From the control points F_1 and F_3, the coal basin has been defined using an elliptical curve and the maximum depth found at point F_2.

An alluvial deposit of finite extent (domain 1) is thus defined (Fig. 6, bottom). The BEM computation is performed in the frequency domain by considering plane incident SH waves. The influence of the radiation pattern of the source may be strong [14,35,36] and a detailed analysis of this issue should be considered. Nevertheless, since the recordings correspond to various sources (averaged results), the influence of the source location and type was disregarded and we have only considered plane wave excitation in the simulations. In our BEM mesh, the smallest boundary element size is chosen as 3 m along the free surface, allowing computations up to 20 Hz. Time domain solutions are computed afterwards from frequency responses by using the inverse Fourier transform.

The mechanical features of the basin and the bedrock are the following: shear wave velocity in the basin (domain 1) $V_{S1}=250$ m/s, shear wave velocity in the bedrock (domain 2) $V_{S2}=1200$ m/s. Maximum depth of the surficial layer is 11 m.

6.2. Amplification factors estimated numerically

The amplification level corresponds to the spectral ratios between the ground motion at the free surface and the outcrop motion (i.e., motion at the top of the bedrock when there is no alluvial deposit). The spectral amplification along the North–South profile is plotted in

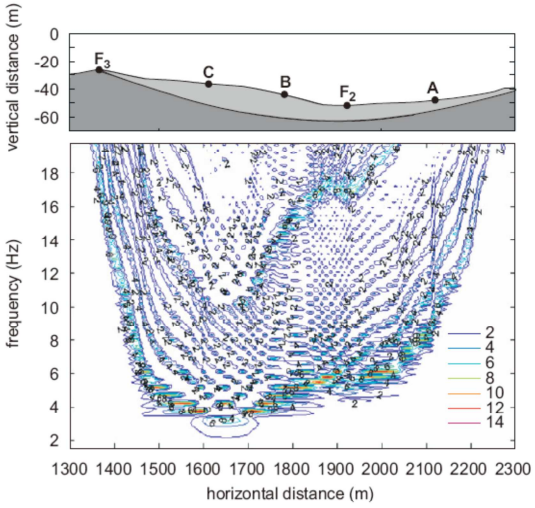

Fig. 7. Amplification factor in the Gardanne coal basin as a function of position and frequency.

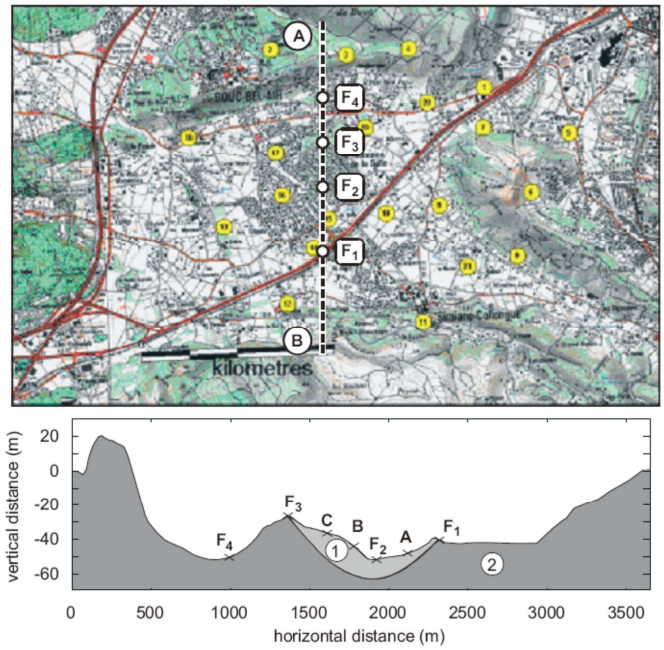

Fig. 6. North–South profile and location of the four drillings F1, F2, F3 and F4 (top) and 2D geological model considered for the boundary element method (bottom).

Fig. 7 as a function of distance (between F_3 and F_1) and frequency (1.5–20 Hz).

The largest amplification ($A=14$) is reached at $f=4.6$ Hz and $d=1500$ m, at $f=4$ Hz and $d=1550$ m and also at $f=3.9$ Hz and $d=1580$ or 1720 m. For the same mechanical and geometrical features, a 1D model leads to a fundamental frequency $f=5.7$ Hz and a spectral amplification $A_0=7$ (Eq. (6)). Due to basin edge effects (trapped surface waves), the 2D amplification computed by the BEM is larger than the 1D amplification.

In Fig. 6 (bottom), five points were identified along the basin surface: F_1, $d_1=2314.8$ m; A, $d_A=2107.2$ m; F_2, $d_2=1902.4$ m; B, $d_B=1691.2$ m; C, $d_C=1499.3$ m. For these points, the transfer functions (outcrop motion) are displayed in Fig. 8 and lead to the following results:

- At point F_1, a low motion amplification is obtained: around $A=1.4$ for $f=5.5$ Hz. For the F_1 drilling location, the depth of the surficial layer is nearly zero and the amplification is thus small;
- At point A, the spectral amplification is nearly 12.5 at $f=7.5$ Hz;
- The largest amplification (14) is found above drilling F_2 at frequency $f=5.62$ Hz (this frequency value being close to the 1D fundamental frequency);
- At point B, the frequency of maximum amplification is $f=3.8$ Hz and the amplification level is around 9.2;
- Finally, at point C, the maximum amplification (8.8) is reached at $f=8$ Hz.

The maximum amplification derived from the 2D BEM model thus reaches 14 and is larger than the one estimated from the 1D solution (i.e., 7.7). This difference is mainly due to basin edge effects leading to trapped surface waves [32]. Finally, the order of magnitude of spectral amplifications estimated numerically is in the same range as the one of spectral ratios obtained from the recordings (Fig. 2).

6.3. *Amplification of synthetic wavelets*

To investigate the motion amplification in the time domain, a 2nd order Ricker wavelet is now considered for the incident motion. The 2nd order Ricker wavelet corresponds to the 2nd derivative of a Gaussian [14] and it is well localized both in time and frequency. The fundamental period of the Ricker wavelet is $t_p=0.32$ s related to a fundamental frequency $f_p=3.12$ Hz.

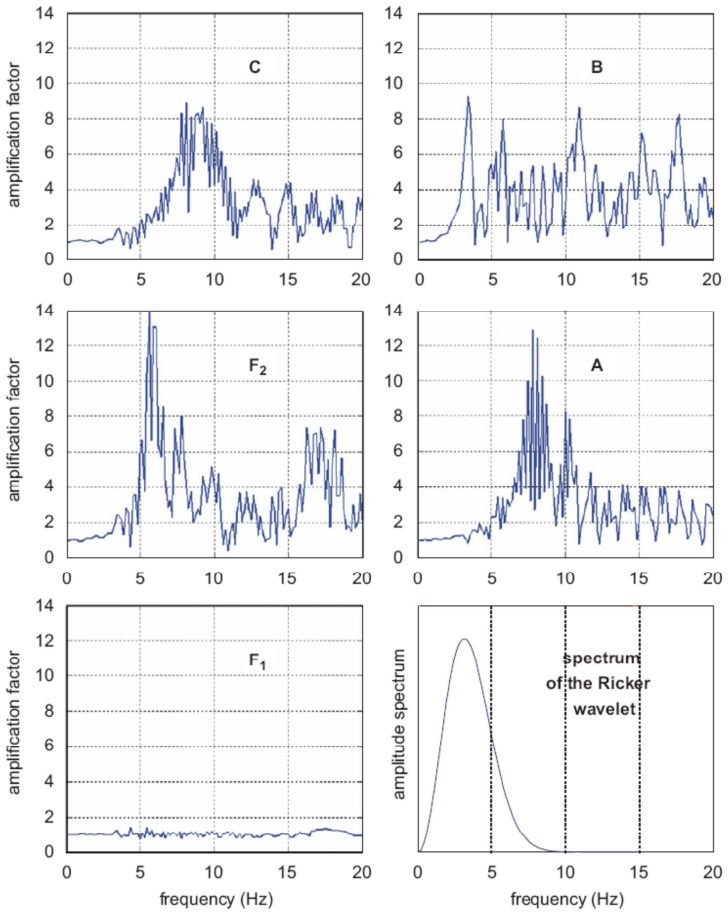

Fig. 8. Transfer function (outcrop motion) for five different points along the deposit (F_1; A; F_2; B; C, see Fig. 6) and spectrum of the Ricker wavelet used hereafter for the time-domain analysis (bottom right).

Its amplitude spectrum is given in Fig. 8 (bottom right) with the transfer functions.

Using the Fourier transform of the Ricker wavelet and the transfer functions at the five different points along the free surface (Fig. 8), the ground motion at each point is determined in the time domain.

The time domain response is normalized by the amplitude of the incident Ricker wavelet $\overline{u} = u/u_0$ and plotted in Fig. 9. The lowest amplification is found at point F_1 where only the free surface effect is observed ($\overline{u} = u/u_0 = 2$ due to the reflection). The largest amplification is reached at point F_2 ($\overline{u} = 4.09$) and point B ($\overline{u} = 4.71$) (Fig. 9). When comparing the transfer functions at points F_2 and B at the fundamental frequency of the Ricker wavelet, $f_p = 3.12$ Hz (Fig. 8), the spectral amplification at point B is larger than that at point F_2. The time domain amplification would have been larger at point F_2 for a Ricker wavelet with a larger fundamental frequency. At both points, a strong increase of the motion duration is also observed (Fig. 9). It is not the case at points A and C where the amplification is low and the motion duration is hardly amplified.

6.4. *Amplification from actual signals*

6.4.1. *Reference motion at the basin edge (point F_1)*

To compute the ground motion using actual recordings, it is mandatory to get a reference outcrop motion in order to combine it with the transfer functions at each point along the basin. However, since it is often difficult to have a good outcrop reference site, the reference motion may also be obtained by deconvoluting a recorded surface motion using the transfer function at this point (it must have been computed in an accurate way). From the reference signal, the ground motion may then be computed all along the alluvial deposit.

As shown in Fig. 8, the transfer function at point F_1 is very flat and very close to 1 (low amplification). The ground motion at this point may thus be considered as the reference motion in order to compute the surface motion inside the basin. Since the BEM computations involve SH waves (y-polarization normal to the model plane), the acceleration component a_y is chosen. The reference outcrop acceleration a_y at point F_1 is displayed in Fig. 10. It has been weighted by a Hamming window and the peak acceleration is 0.155 m/s^2.

6.4.2. *Recorded motion at the basin center (point F_2)*

The three components of the ground motion recorded at the center of the basin (point F_2) are displayed in Fig. 11 in terms of particle velocity (left) and acceleration. The amplitude of the particle velocities is small compared to seismic motions (PGV = 10 mm/s). The largest acceleration is reached along y: $a_y = 0.407$ m/s^2. In the following, the ground motion will be computed for different points along the basin.

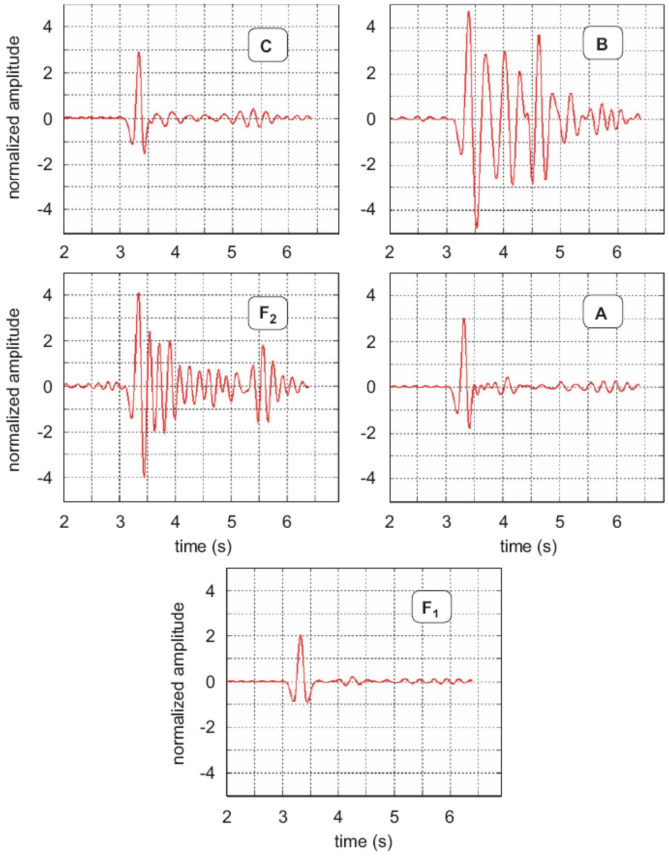

Fig. 9. Ground motion at the free surface due to an incident Ricker wavelet.

6.4.3. Numerical estimation of the ground motion in the basin

Using the reference motion (Fig. 10) and the numerical transfer function at the points located in the basin (Fig. 8), the ground motion at the following 4 sites is computed: F_2, A, B and C (Fig. 6). Denoting $S_{F_1}(\omega)$ the Fourier spectrum of the recorded motion at F_1 (location with no amplification), the spectrum $S_M(\omega)$ of the motion at any point M along the profile may be computed by using the transfer function $H_M(\omega)$ at this point in the following way:

$$S_M(\omega) = S_{F_1}(\omega) H_M(\omega) \tag{8}$$

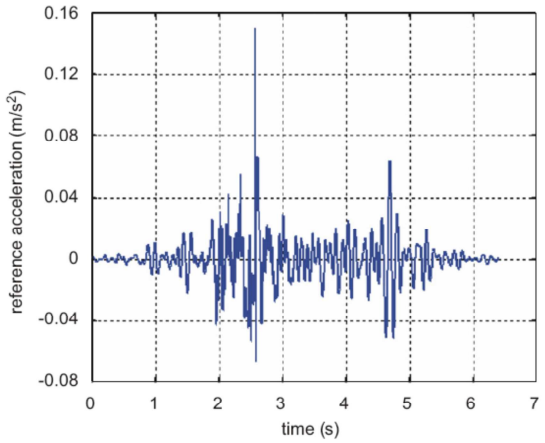

Fig. 10. Reference outcrop acceleration a_y at the basin edge (point F_1).

First of all, it is checked that the acceleration computed at F_2 matches the recorded signals displayed in Fig. 11. Combining the reference motion at F_1 (Fig. 10) and the transfer function computed by the BEM at F_2 (Fig. 8) for the y component of acceleration, the amplified acceleration at F_2 is obtained. As displayed in Fig. 12, the time history of the computed acceleration (y component) is very close to the acceleration signal recorded at F_2 (Fig. 11, center right). At point F_2, the maximum acceleration along y is found to be 0.407 m/s^2 leading to an amplitude ratio of 2.63 when compared to the maximum acceleration in F_1. As usual, the time domain amplification is lower than the spectral amplification [14].

For points A, B and C, no recordings are available but similar computations are possible. The y component of acceleration is computed at each point and the Peak Ground Acceleration (PGA) is compared to that obtained at point F_1. As shown in Table 1, the amplification is around 35% at point A (0.210 m/s^2 instead of

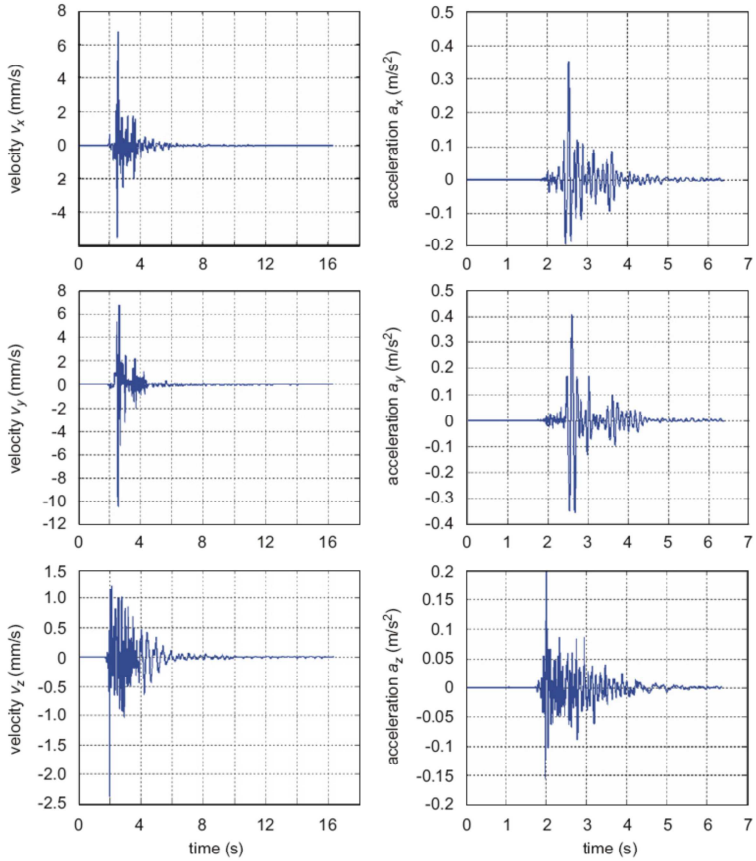

Fig. 11. Components of the particle velocities (left) and accelerations (right) recorded at the basin center (point F_2).

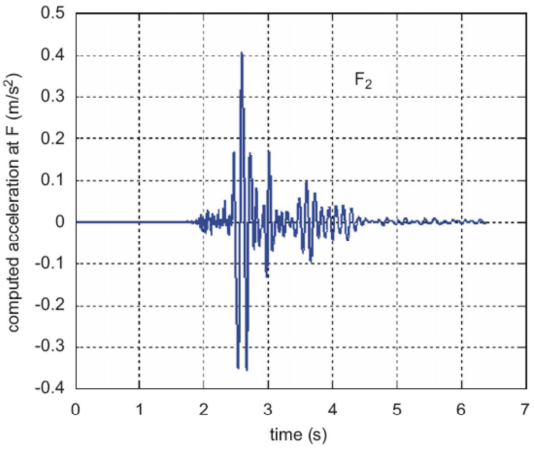

Fig. 12. Acceleration at point F_2 computed from the reference signal at F_1 and the transfer function at F_2.

Table 1
Peak ground acceleration computed at different points and related amplifications.

Locations	PGA (m/s^2)	Amplification/F_1
Point F_1	0.155	
Point A	0.210	1.35
Point B	0.220	1.42
Point C	0.190	1.23
Point F_2	0.407	2.63

0.155 m/s^2 at F_1). At point B, the acceleration is slightly larger than at point A (amplification: 42%). At point C, the reference signal is amplified by around 20% only. The largest amplification (amplitude ratio: 2.63) is reached at point F_2, which is located over the deepest part of the deposit (Table 1).

As already mentioned, the time domain amplification is lower than the spectral amplification. However, as shown by the transfer functions at different points (Fig. 8), the amplification process is strongly influenced by the frequency content due to the depth variations in the deposit.

Finally, the amplification of the time signal is higher at points located over the alluvial deposit, which confirms the results obtained from the measurements [1], showing that the amplification is larger at points located in the vicinity of the center of the deposit.

7. Conclusion

The propagation and amplification of mine induced vibrations were studied numerically by the boundary element method. Surficial alluvial deposits are found to amplify the incident motion, which may lead to stronger excitations of the buildings located at the surface. A parametric study for various types of alluvial basins has been performed in order to make our numerical results applicable for different sites. The results provide the estimation of the amplification level and of the related frequency depending on both the shape ratio and the shear wave velocities ratio. Narrow basins lead to amplification levels and frequencies very different from the 1D case.

From the estimated geological profile of the Gardanne coal basin, the 2D amplification of the mine induced vibrations is then computed. These effects are found to significantly influence the ground motion at the free surface and thus the dynamic loading on the surface structures (i.e. buildings). For soft or deep surficial layers, the incident motion, even if moderate, may lead to significant ground motion at the surface of the deposit. Since they lead to different types of results, spectral and time domain amplifications must be studied simultaneously.

Future work will focus on the dynamic response of surface structures and the influence of the amplification of the ground motion [38,39].

References

[1] Driad-Lebeau L, Lokmane N, Semblat JF, Bonnet G. Local amplification of deep mining induced vibrations Part 1: Experimental evidence for site effects in a coal basin. Soil Dynamics and Earthquake Engineering 2009;29(1):39–50.
[2] Ben Slimane K, Besson JC, Mandereau G, Chambon C. Seismic Monitoring: A Tool for planning mining sites submitted to dynamic phenomena. 3rd Franco-Polish Symposium, Wroclaw. Vol: XI(1 and 2), 1990, pp. 55–68.
[3] Linkov A, Zoubkov V, Al Heib M. Computer aided analysis of stressed state and rockburst hazard in veins and coal seams influenced by faults. In: Gürtunca RG, Hagan TO, editors. SAREST 97. First Southern African Rock Engineering Symposium. Johannesburg, South Africa, 1997.
[4] Kanelo K, Sugawara K, Obara Y. Rock stress and microseismicity in a coal burst district. In: Fairhurst, editor. Rockburst and Seismicity in Mines. Rotterdam: Balkema; 1999.
[5] Senfaute G, Chambon C, Bigarre P, Guise Y, Josien JP. Spatial distribution of mining tremors and the relations to rockburst hazard. Journal of Pure and Applied Geophysics 1997;150:451–9. Birkhäuser Verlag, Basel.
[6] Senfaute G, Al Heib M, Josien JP, Noirel JF. Detection and monitoring of high stress concentration zones induced by coal mining using numerical and microseismic methods. Rockburst and Seismicity in Mines—South African Institute of Mining and Metallurgy 2001.
[7] Driad-Lebeau L, Lahaie F, ALHeib M, Josien JP, Bigarré P, Noirel JF. Seismic and geotechnical investigation following rockburst in a complex French mining district. International Journal of Coal Geology 2005;64:66–78.
[8] Moczo P, Kristek J, Vavrycuk V, Archuleta RJ, Halada L. 3D heterogeneous staggered-grid finite-difference modeling of seismic motion with volume harmonic and arithmetic averaging of elastic moduli and densities. Bulletin of the Seismological Society of America 2002;92(8):3042–66.
[9] Virieux J. P–SV wave propagation in heterogeneous media: velocity–stress finite-difference method. Geophysics 1986;51:889–901.
[10] Bonilla F. Computation of Linear and Nonlinear Site Response for Near Field Ground Motion, PhD, University of California at Santa Barbara, 2000.
[11] Hughes TJR, Reali A, Sangalli G. Duality and unified analysis of discrete approximations in structural dynamics and wave propagation: comparison of p-method finite elements with k-method NURBS. Computer Methods in Applied Mechanics and Engineering 2008;197(49–50):4104–24.
[12] Ihlenburg F, Babuška I. Dispersion analysis and error estimation of Galerkin finite element methods for the Helmholtz equation. International Journal for Numerical Methods in Engineering 1995;38:3745–74.
[13] Semblat JF, Brioist JJ. Efficiency of higher order finite elements for the analysis of seismic wave propagation. Journal of Sound and Vibration 2000;231(2):460–7.
[14] Semblat JF, Pecker A. Waves and vibrations in soils: earthquakes, traffic, shocks, construction works. IUSS Press: Pavia, Italy; 2009. 500p.
[15] Chaljub E, Komatitsch D, Vilotte JP, Capdeville Y, Valette B, Festa G. Spectral Element Analysis in Seismology. In: Ru-Shan Wu, Valérie Maupin, editors. Advances in Wave Propagation in Heterogeneous Media. Advances in Geophysics, Elsevier, 2007; 48: 365–419.
[16] Faccioli E, Maggio F, Quarteroni A, Tagliani A. Spectral-domain decomposition method for the solution of acoustic and elastic wave propagation. Geophysics 1996;61:255–60.
[17] Komatitsch D, Vilotte JP. The spectral element method: an efficient tool to simulate the seismic response of 2D and 3D Geological Structures. Bulletin of the Seismological Society of America 1998;88:368–92.
[18] Beskos DE. Boundary element methods in dynamic analysis, Part. II (1986–1996). Applied Mechanics Reviews 1997;50:149–97.
[19] Bonnet M. Boundary integral equation methods for solids and fluids. Chichester: Wiley; 1999. 391p.
[20] Dangla P, Semblat JF, Xiao HH, Delépine N. A simple and efficient regularization method for 3D BEM: application to frequency-domain elastodynamics. Bulletin of the Seismological Society of America 2005;95:1916–27.
[21] Semblat JF, Duval AM, Dangla P. Numerical analysis of seismic wave amplification in Nice (France) and comparisons with experiments. Soil Dynamics and Earthquake Engineering 2000;19(5):347–62.
[22] Chaillat S, Bonnet M, Semblat JF. A multi-level fast multipole BEM for 3-D elastodynamics in the frequency domain. Computer Methods in Applied Mechanics and Engineering 2008;197(49–50):4233–49.

[23] Chaillat S, Bonnet M, Semblat JF. A new fast multi-domain BEM to model seismic wave propagation and amplification in 3D geological structures. Geophysical Journal International 2009;177:509–31.
[24] Fujiwara H. The fast multipole method for solving integral equations of three-dimensional topography and basin problems. Geophysical Journal International 2000;140:198–210.
[25] Aki K, Larner KL. Surface motion of a layered medium having an irregular interface due to incident plane SH waves. Journal of Geophysical Research 1970;75:1921–41.
[26] Bouchon M, Campillo M, Gaffet S. A boundary integral equation-discrete wavenumber representation method to study wave propagation in multi-layered media having irregular interfaces. Geophysics 1989;54:1134–40.
[27] Wolf JP. The scaled boundary finite element method. Chichester, UK: Wiley; 2003.
[28] Sanchez-Sesma FJ. Diffraction of elastic waves by three-dimensional surface irregularities. Bulletin of the Seismological Society of America 1983;73(6):1621–1636.
[29] Aochi H, Seyedi M, Douglas J, Foerster E, Modaressi H. A complete BIEM–FDM–FEM simulation of an earthquake scenario. General Assembly of the European Geosciences Union 2005.
[30] Bard PY. Effect of surface geology on ground motion: recent results and remaining issues. Tenth European Conference on Earthquake Engineering, Vienna, Austria 1994; 1: 305–23.
[31] Bouchon M. Effects of topography on surface motion. Bull Seismological Society of America 1973;63:615–22.
[32] Semblat JF, Kham M, Parara E, Bard PY, Pitilakis K, Makra K, Raptakis D. Site effects: basin geometry vs. soil layering. Soil Dynamics and Earthquake Engineering 2005;25(7–10):529–38.
[33] Humbert P, Dubouchet A, Feyzans G, Remaud D. CESAR-LCPC: A computation software package dedicated to civil engineering uses. Bulletin des Laboratoires des Ponts et Chaussées 2005;256–257:7–37.
[34] Bard PY, Bouchon M. The two-dimensional resonance of sediment-filled valleys. Bull Seismological Society of America 1985;75(2):519–41.
[35] Crouch SL. Analysis of stresses and displacements around underground excavations: An application of the displacement discontinuity method. Minneapolis, USA: University of Minnesota publication; 1980.
[36] Rudnicki JW. Energy radiation from a spherically symmetric source. Bulletin of the Seismological Society of America 1983;73(4):901–6.
[37] Gaviglio P, Bigarré P, Baroudi H, Piguet JP, Monteau R. Measurements of natural stress in a provence mine (southern France). Engineering Geology 1996;44:77–92.
[38] Pedersen HA, Campillo M, Sanchez-Sesma FJ. Azimuth dependent wave amplification in alluvial valleys. Soil Dynamics and Earthquake Engineering 1995;14(4):289–300.
[39] Semblat JF, Kham M, Bard PY. Seismic-wave propagation in alluvial basins and influence of site–city interaction. Bulletin of the Seismological Society of America 2008;98:2665–78.
[40] Chávez-García FJ, Raptakis DG, Makra K, Pitilakis KD. Site effects at Euroseistest-II. Results from 2D numerical modelling and comparison with observations. Soil Dynamics and Earthquake Engineering 2000;19(1):23–39.
[41] Sánchez-Sesma FJ, Vai R, Dretta E, Palencia VJ. Fundamentals of elastic wave propagation for site amplification studies. In: Kausel E, Manolis G. (editors). Wave motion in earthquake engineering. WIT Press, Southampton, UK;2000. p.1–36.